UC Berkeley
UC Berkeley Previously Published Works

Title

Atmospheric river lifecycle characteristics shaped by synoptic conditions at genesis

Permalink

https://escholarship.org/uc/item/5mp5v5sn

Journal

International Journal of Climatology, 42(1)

ISSN

0899-8418

Authors

Kim, Sol
Chiang, John CH

Publication Date

2022

DOI

10.1002/joc.7258

Peer reviewed

Atmospheric River Lifecycle Characteristics Shaped by Synoptic Conditions at Genesis

Sol Kim[1] | **John C.H. Chiang[1]**

[1]Department of Geography, University of California, Berkeley, Berkeley, CA, 94720, USA

Correspondence
Department of Geography, University of California, Berkeley, Berkeley, CA, 94720, USA
Email: solkim@berkeley.edu

Funding information
Department of Geography, University of California, Berkeley

The range of synoptic patterns that North Pacific landfalling atmospheric rivers form under are objectively identified using genesis day 500 hPa geopotential height anomalies in a self-organizing map (SOM). The SOM arranges the synoptic patterns to differentiate between two groups of climate modes - the first group with ENSO (El Niño Southern Oscillation), PDO (Pacific Decadal Oscillation), PNA (Pacific North American) and NP (North Pacific index) and the second group with AO (Arctic Oscillation), EPO (East Pacific Oscillation), and WPO (West Pacific Oscillation). These two groups have their positive and negative modes organized in opposite corners of the SOM. The ARs produced in each of the synoptic patterns have distinct lifecycle characteristics (such as genesis and landfall location, duration, velocity, meridional/zonal movement) and precipitation impacts (magnitude and spatial distribution). The conditions that favor AR trajectories closer to the tropics tend to produce higher amounts of precipitation. The large-scale circulation associated with AR genesis shows a close relationship between the genesis location and the location and intensity of the upper-level jet in the west/central pacific as well as anomalous, low-level southwesterly winds in the east pacific.

KEYWORDS
atmospheric rivers, self-organizing maps, genesis

1 | INTRODUCTION

Atmospheric rivers (ARs) are narrow, filamentary structures in the lower atmosphere responsible for transporting the majority of water vapor across the mid-latitudes towards the poles (Zhu and Newell, 1998). These features cover only ∼10% of the Earth's circumference but transport more than 90% of the total poleward atmospheric water vapor transport in the midlatitudes. When these features make landfall, they can be associated with both beneficial and hazardous impacts (Ralph et al. (2006); Ralph and Dettinger (2011); Ralph et al. (2019)). In the state of California, ARs are responsible for 20-50% of the annual precipitation (Dettinger et al., 2011) while simultaneously being responsible for nearly all flood events (Ralph et al. (2006); Florsheim and Dettinger (2015)). As ARs affect a wide-range of sectors, advancing understanding of the modulating dynamics of ARs throughout their lifecycle offers immense potential socioeconomic benefits.

The large-scale dynamics of ARs are an area of active research (Ralph et al. (2017); Gimeno et al. (2014)). Many earlier studies on ARs and large-scale dynamics have tied AR impacts, such as total rainfall or snow water equivalent, to climate indices as opposed to direct detection and tracking of ARs (e.g. Bao et al. (2006); Ralph and Dettinger (2011); Ryoo et al. (2013)). However, with the recent rise in AR detection and tracking algorithms, studies have begun examining dynamics with direct tracking (Shields et al. (2018); Rutz et al. (2019)). One well-established study by Payne and Magnusdottir (2014) investigated the dynamics of North Pacific ARs making landfall along the west coast of North America from Alaska to Mexico. They showed a close relationship in the eastward progression of ARs and the location of the jet as well as Rossby wave breaking. Although they analyzed the lifecycle characteristics of landfalling ARs, it was focused primarily on the landfalling and pre-landfall characteristics and dynamics over the eastern half of the Pacific. Other studies examining landfall and pre-landfall characteristics have focused on relatively short periods (24-72) around landfall (e.g. Neiman et al. (2013); Rutz et al. (2014); Waliser and Guan (2017)) (Zhou and Kim, 2019).

In the context of large-scale dynamics, the formation of ARs and their maintenance are particularly understudied aspects in the AR lifecycle and warrant further research (Gimeno et al. (2014); Benedict et al. (2019); Zhou and Kim (2019)). There are currently only a few very recent studies that have incorporated genesis as part of their study (Payne and Magnusdottir (2014); Gonzales et al. (2019); Sellars et al. (2017); Guan and Waliser (2019); Zhou et al. (2018); Zhou and Kim (2019)). The three studies characterizing genesis locations (Sellars et al. (2017); Guan and Waliser (2019); Zhou et al. (2018)) are all largely consistent in that AR genesis in the North Pacific preferentially occurs near the western boundary of the Pacific basin (near ∼30N, 140E). As for differences, Zhou et al. (2018) finds another area of high genesis near 150W in the subtropics related to 'Pineapple Express' events and Sellars et al. (2017) finds high genesis occurring along the Intertropical Convergence Zone (ITCZ) near the equator. These differences are likely a result of differences in detection and tracking (Shields et al. (2018); Guan and Waliser (2019)). For example, Sellars et al. (2017) did not explicitly search for ARs but rather high IVT features. They thus captured features such as tropical moisture exports and tropical cyclones which are able to produce strong IVT signatures.

As for characteristics, Payne and Magnusdottir (2014) found stronger ARs to have genesis in the western Pacific while weaker ARs to have genesis in the east Pacific. Zhou et al. (2018) found longer lived, farther traveling, and stronger ARs to originate in primarily in the west Pacific while shorter, weaker ARs can originate throughout the Pacific basin. Zhou and Kim (2019) extended their analysis from this study to specifically investigate the impact of genesis location on lifecycle characteristics. The landfalling ARs in their study are separated based on east and west Pacific genesis location and the AR characteristics associated with each genesis region agree with previous studies (Zhou et al. (2018); Guan and Waliser (2019)). They additionally composite geopotential height anomalies and find significant differences for the two origin locations. Guan and Waliser (2019) found genesis location to impact a variety of characteristics such as lifetime, distance traveled, net displacement, speed, and direction consistent with Zhou

et al. (2018). Guan and Waliser (2019) specifically notes the processes determining AR lifecycle characteristics needs further investigation. Gonzales et al. (2019) investigated AR temperature trends by generating genesis to landfall AR tracks for individual ARs that impact the west coast of the U.S. They found along-track temperatures, coastal SSTs, and background regional temperatures to have varying degrees of influence on AR temperatures which in turn can have important hydrological impacts such as rain/snow precipitation fractions, water resources, and flood risks. This study, along with others (Zhou and Kim (2019); Guan and Waliser (2019)), reveals the importance of understanding AR lifecycle characteristics, such as genesis and track locations, as these can influence the landfalling AR impacts. We employ the AR track catalogue used in Gonzales et al. (2019) along with Guan and Waliser (2019)'s catalogue for this study and look to identify what large-scale atmospheric patterns AR genesis occurs under.

Fig. 1 displays a composite of 500 hPa geopotential height anomalies occurring on the genesis day of all U.S. west coast landfalling ARs (November - February, 1980-2015) from the Gonzales AR catalogue. A deepened Aleutian low with positive height anomalies to the west over the higher latitudes of the central Pacific can be seen but this composite view masks the wide range of conditions under which AR genesis can occur. Differences in large-scale circulation at and just prior to landfall have been shown to produce varied ARs (such as strength, trajectories, landfall locations, orientations) and hydrological impacts (Payne and Magnusdottir (2014); Guirguis et al. (2019); Neiman et al. (2008); Zhang and Villarini (2018); Swales et al. (2016); Ryoo et al. (2015); Ryoo et al. (2013); Hu et al. (2017)). These studies show that there are significant differences in the types of ARs that make landfall and the large-scale circulation associated with them. This highlights a present challenge of studying the large-scale dynamics of ARs; for example, subsetting ARs based on the strength of ARs alone or taking subsets of ARs making landfall over a specific region/latitude can contain ARs that are very dynamically different.

As the formation and maintenance of ARs remains understudied and given that ARs are heterogenous in their controls, the objectives of this study are to explore: i) What is the range of synoptic conditions that lead to AR genesis? ii) Do these large-scale circulation patterns generate ARs with different lifecycle characteristics? and iii) How do these characteristics translate into variable precipitation impacts at landfall? We investigate the range of synoptic conditions, and their associated climate modes, that ARs form under by utilizing self-organizing maps (SOM) (Kohonen (1982a); Kohonen (1982b)) trained on AR genesis days for 500 hPa geopotential heights. We show how these synoptic differences affect AR lifecycle characteristics from genesis to landfall and how these characteristics translate into precipitation impacts downstream. This study follows the SOM methodology used in Guirguis et al. (2019) to categorize distinct types of ARs by their circulation pattern at landfall for 40N in northern California.

The structure of this paper is as follows. In Section 2, the reanalysis data set, climate indices, AR track catalogues, and the SOM method are described. The organization of the SOM map and the differentiated AR characteristics and impacts associated with the synoptic patterns are presented in Section 3. Discussion and conclusions are presented in Section 4. Finally, the Appendix and Supporting Information are contained in Section 5 and Section 6 respectively.

2 | DATA AND METHODS

2.1 | Reanalysis Data Set

In this study, reanalysis data from MERRA-2 (Modern Era Retrospective analysis for Research and Applications, version 2) (Gelaro et al., 2017) is analyzed from 1980 to 2015 at a spatial resolution of ~50km ($0.5°$x$0.625°$) and a daily temporal resolution. The 500 hPa geopotential height (zg) field is used for the SOM analysis with resolution coarsened to ~250km ($2.5°$x$2.5°$) for the SOM training as performance is sped up without meaningful differences in the resulting SOM. We remove the seasonal cycle for each grid point to generate anomalies and then standardize (center to 0 with

a standard deviation of 1). The daily temporal resolution and the coarser grid are appropriate for this SOM analysis considering the synoptic scale; we are interested in investigating which large-scale patterns are conducive for AR genesis over many years.

Along with geopotential height, the other variables used in this study for precipitation and large-scale circulation analysis are: integrated vapor transport (IVT), precipitation (pr), zonal wind (U) at 250 hPa, potential vorticity (PV) at 200 hPa, and wind (U and V) at 825 hPa. IVT is integrated from 1000 hPa to 200 hPa. IVT was processed and obtained from ARTMIP (Atmospheric River Tracking Method Intercomparison Project) (Shields et al., 2018) and is calculated using equation 1:

$$IVT = -\frac{1}{g} \int_{P_b}^{P_t} (q(p)\mathbf{V}_h(p)) dp, \tag{1}$$

where q is the specific humidity ($kg\,kg^{-1}$), $\mathbf{V}_h$ is the horizontal wind vector (ms^{-1}), P_b is 1000hPa, P_t is 200hPa, and g is the acceleration due to gravity. The composite geopotential heights shown in Fig. 2 are generated with the anomalies without standardization. We use a spatial domain from 10N-65N, 110E-255E for our SOM analysis and most of our composites. The composites show latitude lines at 30N and 60N and the longitude lines at 120E, 180E, and 240E (shown and labelled in Fig. 1). This domain sufficiently captures the AR genesis and termination locations along with the dynamics affecting ARs.

2.2 | AR Track Catalogue

The primary AR catalogue utilized in this study was generated by Kyle Nardi in Gonzales et al. (2019). This catalogue is based on the Mundhenk AR algorithm (Mundhenk et al. (2016); Shields et al. (2018)) but is adapted to incorporate tracking (not just detection) and filtered to include only ARs making landfall along the U.S. west coast (California to Washington) from landfall back to genesis. The Mundhenk algorithm uses a relative threshold (94th percentile) for IVT anomaly values for detection. The adaptation for tracking uses a Lagrangian approach to track AR objects back in time through consecutive time steps. There are additional geometric constraints to filter out cyclone-like features (>1400km length, aspect ratio 1:4). It should be emphasized non-landfalling ARs and ARs making landfall poleward of Washington and equatorward of California are not considered in this dataset. This catalogue begins in Jan 1980. We analyze from 1980 to 2015 during the core wet season months of Nov-Feb when ARs peak seasonally for the U.S. west coast (Mundhenk et al., 2016). For this time period, the catalogue records landfalling ARs for the west coast of the U.S. Each of these ARs has an associated track, recording date and time, latitude, and longitude from landfall back to genesis. The latitude and longitude coordinate is based on the IVT-weighted centroid associated with the AR. We further filter the ARs to consider only those that exist 12 or more hours and end up with 1027 total landfalling ARs for our 36 year period (~28.5 ARs per wet season which agrees with previous studies (Payne and Magnusdottir (2014); Zhou and Kim (2019)). This dataset clearly identifies the initial landfall days associated with each event and thus allows us to investigate landfall impacts. We henceforth refer to this dataset as the 'Gonzales' dataset and all the results in Section 2.1, unless specifically noted, will refer to the Gonzales dataset.

The secondary AR catalogue used is from the widely used AR algorithm developed by Guan and Waliser. The details of this algorithm are discussed in Guan and Waliser (2015) and Guan and Waliser (2019). We include further description and an analysis of this dataset in Section 5 to examine how a purely landfalling AR dataset compares to a dataset that considers all ARs - landfalling or not. We henceforth refer to this dataset as the 'GW19' dataset.

2.3 | Climate Indices

As we are interested in the synoptic patterns associated with AR genesis we use a variety of tropical and extratropical large-scale climate modes that affect the Pacific atmosphere: El Niño Southern Oscillation (ENSO), Pacific Decadal Oscillation (PDO), Pacific North American pattern (PNA), North Pacific index (NP), Arctic Oscillation (AO), West Pacific Oscillation (WPO), and East Pacific Oscillation (EPO). These are all the large-scale modes examined in Guirguis et al. (2019), with the addition of the NP index. For ENSO, we use the Oceanic Niño Index (ONI).

For conciseness, we will refer to the ONI, PDO, PNA, and NP modes collectively as the 'ENSO modes' throughout the rest of the paper as these modes generally organize on the SOM map similarly (Section 3.1) and are known to have strong associations with ENSO. These modes track low frequency variations on timescales ranging from decadal (e.g. PDO) to interannual (e.g. ONI and NP); PNA may be the exception which can capture subseasonal variations. As with the ENSO modes, we will group the AO, WPO, and EPO modes together and refer to them collectively as 'jet modes' as they also organize similarly on the SOM (Section 3.1) and for their strong influence on the jet over the Pacific. The jet modes track variations at the subseasonal scale.

The temporal resolution of the indices' records are either daily or monthly. In the monthly cases, daily indices were generated simply by using the monthly value for each day within the month. The temporal resolution of each mode and the sources of data are summarized in the Table 1. We standardize the indices to be centered at 0 and have a standard deviation of 1. We also include the distribution of Madden-Julian Oscillation (MJO) phases related to AR genesis in Fig. S1 Section 6.

2.4 | Self-Organizing Maps

SOM analysis (Kohonen (1982a); Kohonen et al. (2001)) is an unsupervised learning technique based on artificial neural network models that has received considerable attention and demonstrated applications in meteorology and climatology including extreme events (Hewitson and Crane (2002); Sheridan and Lee (2011); Skific and Francis (2012); Gibson et al. (2017); Liu and Weisberg (2011)). In many respects, SOMs are analogous to more traditional forms of cluster analysis. A SOM arranges nodes into a 2-dimensional array where similar nodes are located close together in the array and dissimilar nodes are further apart. Thus, in opposite corners, the nodes with the largest differences will be mapped (Sheridan and Lee, 2011).

There are several AR studies that have incorporated SOM analysis. Swales et al. (2016) and Radić et al. (2015) used SOMs trained on IVT to determine the different moisture pathways on the U.S. west coast and to examine the future changes, as projected by CMIP5 models, in ARs making landfall over British Columbia respectively. In contrast to IVT, SOMs trained on geopotential heights were used to study the synoptic scale patterns associated with both landfalling ARs near the Russian River in California (Guirguis et al., 2019) and flood events throughout the U.S. (Schlef et al., 2019). In this study, we employ SOM analysis on geopotential heights to similarly examine the synoptic patterns and climate modes associated with AR genesis in the North Pacific. We include an overview of how the SOM is trained as well as parameter choices in Section 5.1.

3 | RESULTS

3.1 | Synoptic Patterns of AR Genesis

In this section, we will use self organizing maps (Fig. 2) through the lens of climate indices (Fig. 3) to understand the range and organization of synoptic conditions that lead to the genesis of ARs that make landfall on the U.S. west coast (Gonzales dataset). Generally, for the ENSO modes (ONI, PDO, PNA, and NP), the nodes are organized with a positive to negative phase gradient going from the top left (Node 1) to bottom right (Node 9). These 4 indices are generally in phase and the top left corner nodes (Nodes 1,2,4) are all positive/neutral while the bottom right corner nodes (Nodes 6,8,9) are all negative.

ONI, PDO, and NP (PNA) have their most positive values at Node 1 (Node 4). ONI and PDO (PNA and NP) exhibit strongest negative phasing at Node 6 (Node 9). The synoptic pattern for Node 1 captures familiar boreal winter geopotential height anomalies associated with positive ENSO, PDO, and NP phases; the Aleutian low is deepened with low anomalies extending westward and northward over Siberia and high anomaly heights over Japan, south of the Aleutian low, and over the western U.S. Node 4, which represents the most positive phase of PNA, has a low anomaly similar to Node 1 but the secondary low is shifted toward the western Pacific over Japan. High anomalies are seen over western North America and in the polar latitudes over Siberia. The negative phase for all 4 of these modes are characterized by high pressure anomalies over the central Pacific as can be seen in Node 9 and 6; Node 9's high pressure anomaly has a greater extent and magnitude. For both of these nodes, the high pressure anomaly is surrounded by weaker, low pressure anomalies.

Meanwhile, the jet modes (AO, WPO, and EPO) are generally in phase with the positive to negative phase gradient going from top right (Node 3) to bottom left (Node 7). These 3 indices are all positive/neutral in the top right corner (Node 2, 3, 6) while the bottom left corner nodes (Nodes 4, 7, 8) are all negative/neutral. WPO and AO have their highest (lowest) value at Node 3 (Node 7) and EPO has its highest (lowest) value at Node 2 (Node 7). The respective most positive nodes for these three indices reflect differences in typical anomalies associated with the indices. Node 3 (WPO and AO's most positive) and Node 2 (EPO's most positive) show the low anomaly center in the western/central and eastern regions of the North Pacific respectively. When these modes are positive, the jet tends to be shifted northward. The most negative node for these modes (Node 7) combines features from Node 2 and 3 but with the sign of the anomaly reversed. The high pressure ridge is characteristic of the negative phases of these modes and is associated with an equatorward shifted jet stream.

The center node (Node 5) of the SOM has a weaker overall anomaly composite relative to the other nodes. Additionally, the climate indices do not respond strongly to this node with perhaps the exception of NP. This is not unexpected due to the small size of the SOM map; at the beginning of the ordering phase training, any update to any of the 9 nodes will affect the center node due to the neighborhood radius and thus, there may be several different and competing synoptic patterns grouped to form Node 5's composite. However, this was the tradeoff for ease of interpretation and analysis versus increasing the SOM order. We include the synoptic patterns at landfall (Fig. S4) in Section 6 to show differences compared to genesis.

While the focus of this study is on U.S. west coast landfalling ARs, we note similarities and differences in the SOMs produced by the Gonzales dataset and the GW19 dataset. More detail and figures (Fig. S2 and Fig. S3) found in Section 5.2.

Next, we determine how often the Gonzales SOM synoptic conditions occur during the cool season (defined here as Nov-Feb). We match each cool season day's geopotential height field to the best matching node in Fig. 4a. Frequency analysis of all the cool season days reveals that Node 5 is most similar to climatology as it has the highest

frequency of cool season days that match (12.8%). As previously stated, Node 5's anomalies are the weakest compared to other nodes. In fact, Nodes 2, 3, 5, and 6 all generally have weaker anomalies relative to the other nodes and have a higher frequency of cool season days that match. Node 1 has the lowest frequency at 8.8% which means it is the most uncommon synoptic pattern out of all the nodes. Overall, the left column and bottom row nodes (Nodes 1, 4, 7, 8, and 9) have lower occurrences during the cool season while the top right and center nodes (Nodes 2, 3, 5, and 6) occur more commonly. However, if we examine the frequency of AR genesis occurring on the cool season days that match each respective node (i.e. how often certain synoptic condition generate ARs) (Fig. 4b), Node 1's frequency has by far the largest at 30.0% while Node 5's frequency is the lowest at 20.2%. This means that, while the synoptic conditions associated with Node 1 occur the least frequently throughout the cool season, when it does happen to occur, 30.0% of the time, it produces an AR.

3.2 | AR Characteristics

In the following section, the different AR characteristics associated with the nodes of the SOM are presented. We focus primarily on the corners of the SOM for their ability to represent positive and negative phases of the ENSO modes and the jet modes. These corners also represent the most dissimilar nodes within the SOM. Various average AR metrics were extracted from the AR tracks which can be seen in Table 2. The genesis and landfall coordinates are based on the IVT weighted centroids of the AR object. This explains why the landfall coordinates do not lie precisely on the coast.

The representative nodes of the ENSO modes (Node 1 for positive, Node 9 for negative) produce ARs with several significant differences (significance implied for all comparisons unless specifically noted as not significant; t-test for unequal means, 95% confidence). The average genesis longitude for Node 1 compared to Node 9 is further west by 22°. In fact, Node 9 has genesis occurring closest to the west coast compared to all other nodes. Node 2, another strongly positive large-scale mode node, is 24° further west and has the most western genesis longitude. The genesis latitude only varies by about 1° between the positive (32.3N) and negative (31.1N) phases (not significant). Landfalls occur 2° more poleward and 2.2° more westward when ENSO modes are positive. Landfall longitudes further off-coast can suggest ARs of larger size as the coordinate is determined by the IVT weighted centroid of the AR object. If we compare the most positive (Node 1) and negative (Node 6) ONI nodes, landfall is further south (though not significant) during El Niño compared to La Niña which is expected (Payne and Magnusdottir (2014)). The duration, distance traveled, and AR speed are much longer (>24 hrs), farther (>1.5x), and faster (12.1km/hr) under positive ENSO modes. The negative phase node (Node 9) has the lowest duration, shortest distance, and slowest speed compared to all other nodes. The average latitude of the AR tracks only vary by 0.9 degs (with Node 9 more poleward) but the average longitude of the AR tracks is much further east (with Node 9.4° further east) when the ENSO modes are negative owing to the genesis occurring much closer to the west coast of the U.S. In addition, the zonal displacement is more than x1.5 larger between the positive (Node 1) and negative (Node 9) nodes while meridional displacement is similar (not signficantly different). This causes these two nodes to have the most zonal (Node 1) and meridional (Node 9) ratios amongst all nodes.

The representative nodes of the jet modes (Node 3 for positive, Node 7 for negative) also produce ARs with different characteristics. Genesis occurs at the lowest latitude for the negative jet mode node compared to all the other nodes and is 2° equatorward compared to positive jet mode node. The genesis longitudes are both located quite far west with the positive mode 3.6° further east (not significantly different). Landfall longitude is 3° eastward and closer to the coastline for the positive phase suggesting smaller ARs. The velocity of the negative phase node ARs is 5.5 km/hr faster than the positive phase node ARs. Duration and distance are not significantly affected. These

two nodes however, have the most poleward (positive phase Node 3) and equatorward (negative phase Node 7) average track latitudes producing the greatest difference in track latitudes (2.9°) compared to any other node pair. The average track longitudes only vary by 2.2° with the negative phase further east. The positive and negative modes have similar zonal displacements (not significantly different) but differ in the meridional displacement; the positive phase has much less meridional displacement (2.5°). This leads to pronounced differences in their ratios with the positive phase producing more zonal ARs trajectories and the negative phase producing more meridional trajectories.

While the Gonzales and GW19 datasets catalogue different sets of North Pacific ARs, interestingly, much of the characteristics associated with the nodes is consistent between both datasets. More details are included in Section 5.2.

To summarize the AR characteristics, the ENSO phases strongly affect the longitudinal position of genesis, lifecycle duration, distance traveled, velocity of the AR, and the zonal displacement of trajectories. When the ENSO modes are positive versus negative, ARs tend to originate from the central or west Pacific, last longer, travel further, move faster, and tend to have zonal trajectories. The jet mode phases strongly affect genesis latitude, track latitude, and meridional displacement as well as velocity, although to a lesser degree than the ENSO mode phases. When the jet modes are positive versus negative, ARs tend to have genesis at higher latitudes, travel at higher latitudes, tend to have more zonal trajectories, and move slower. These characteristics, and other factors including local topography, contribute to hydrologic impacts such as how much precipitation will occur (Hughes et al. (2014); Hu et al. (2017); Hecht and Cordeira (2017); Neiman et al. (2011)).

3.3 | Precipitation Impacts

Next, we examine the IVT and precipitation magnitude and distribution using the landfall days of every AR event associated with each node. For instance, if an AR has genesis on Dec. 1 and makes landfall on Dec. 3, then the Dec. 3 date is used for the landfall composites. The IVT and precipitation associated with each node is shown in Fig. 5 and Fig. 6. The IVT shown in Fig. 5 is the raw IVT, not the anomaly, on the day of landfall. The precipitation shown in Fig. 6 is the anomaly over 2 days; the landfall day and the following day. This was done to capture the precipitation from ARs that may have landfall durations that span across more than 1 day.

Generally, the top right nodes (Nodes 2, 3, and 6) and the center node (Node 5) produce smaller amounts of precipitation while the left (Nodes 1, 4, 7) and bottom (Nodes 7, 8, 9) edge nodes produce more precipitation. The spatial distribution of precipitation also varies amongst the nodes. Nodes 1, 4, and 9 tend to produce more precipitation over California and just off-shore over the Pacific compared to all the other nodes which have the biggest precipitation anomalies over Oregon and Washington. The weaker precipitation nodes in the top right (Nodes 2, 3, 6) accordingly have the weakest IVT signatures just off coast. The IVT signature of these nodes also tends to be quite zonal; the other nodes, which produce stronger precipitation on the west coast, have a relatively southerly or southwesterly IVT orientation at landfall. Lastly and importantly, the weak precipitation nodes have the most poleward average latitude for their trajectories. Nodes with synoptic patterns conducive for AR trajectories to reach further equatorward are favorable for stronger precipitation to the west coast.

In Fig. 7a, we take a difference with the positive phase node (Node 1) and negative phase node (Node 9) for the ENSO modes. ARs that form when ENSO modes are positive deliver more precipitation to northern California, Washington and poleward of Washington (Canada to Alaska). Southern/central California and parts of the U.S. interior experience precipitation deficits. While the positive phase node (Node 1) delivers more precipitation overall across the west coast domain compared to the negative phase node (Node 9), both of these nodes deliver relatively large amounts of precipitation compared to the other nodes.

276 The expectation of El Niño precipitation compared to La Niña is for most of California to be wetter while Oregon
277 and Washington are drier. Although this pattern is not represented using the corner nodes (Nodes 1 and 9), it emerges
278 if we subtract the most El Niño node (Node 1) and the most La Niña node (Node 6) as seen in Fig. S5 in Section 6.

279 Taking the difference for the positive (Node 3) and negative (Node 7) phase nodes for the jet modes produces Fig.
280 7b. When the jet modes are positive compared to negative, precipitation is weakly enhanced for southern California
281 while in northern California and the PNW, precipitation shows strong negative anomalies. Examining the IVT associ-
282 ated with these nodes (Fig. 5), over the central Pacific, the negative phase node (Node 7) IVT curves slightly towards
283 the equator while the positive phase node curves poleward leading to much stronger IVT values over the eastern
284 Pacific for the negative mode. Examining the IVT at Hawaii's longitude, Node 7's IVT signature nearly overlaps Hawaii
285 at its southern flank while for Node 3, the IVT signature is north of Hawaii by ∼15°.

3.4 | Large-scale circulation

287 In this section, we examine the large-scale circulation associated with the nodes in the SOM to show the relationship
288 of AR genesis to the upper-level jet and low-level winds. From Fig. 8, areas corresponding to the genesis locations for
289 each node have enhanced IVT values, particularly for the west and central Pacific genesis locations. Fig. 9 anomalies
290 reflects the low-level circulation changes due to the geopotential height anomalies. From Fig. 10, clear differences in
291 the strength and position of upper-level jet can be seen amongst the various nodes. The organization of these winds
292 correspond to the typical jet patterns associated with the ENSO modes and jet modes. Generally moving from top
293 to bottom on the SOM, the jet tends to retract westward and become weaker while moving from left to right on the
294 SOM, the jet becomes more variable. Node 1 shows a clear example of a strong, zonal jet and Node 9 shows a weak,
295 variable jet. Along with these jet changes, the PV gradient in the central Pacific goes from strong to weak moving
296 from the left to the right nodes (Fig. 11). The PV field at landfall is included in Section 6 (Fig. S9).

297 A deepened Aleutian low and strong PV gradient aloft during the positive ENSO modes supports a strong and
298 zonal jet while the negative phase is characterized with a weaker, less zonal jet due to high pressure anomalies over
299 the central Pacific and PV intrusions into the subtropics. The PV gradient is much weaker in the negative ENSO
300 mode. The jet and upper-level PV conditions between positive and negative ENSO modes are consistent with Ryoo
301 et al. (2013). When the jet modes are positive, the jet is aimed slightly northward with a poleward curve while during
302 negative jet modes, the jet is curved more towards the equator due to the high latitude high pressure over the central
303 Pacific. Focusing on Hawaii, the difference in jet position becomes obvious for the positive (Node 3) and negative
304 (Node 7) jet modes. During the negative jet modes, the jet tends to curve much closer to the tropics, allowing the jet
305 stream to penetrate to lower latitudes where moisture is more abundantly available.

306 During positive ENSO modes (Node 1), genesis occurs along the core of the strong upper-level jet over the west
307 and central Pacific. Genesis also occurs on the equatorward flank of the enhanced Aleutian low in the eastern Pacific
308 which corresponds with low-level westerly or southwesterly winds. During negative ENSO modes (Node 9), genesis
309 locations are less constrained, especially latitudinally, with very few ARs forming with the weak, retracted jet over
310 west Pacific and the vast majority forming in the central Pacific and close to the coastline. The upper-level jet is
311 overall weak and variable (suppressed over the central Pacific by the high pressure anomaly) over the central and east
312 Pacific compared to the positive mode. The genesis locations in the eastern Pacific correspond to relatively weak
313 southwesterly winds near the moist tropics in the negative modes.

314 During positive jet modes, genesis occurs all along the straight and slightly poleward tilted jet core. On the
315 southern flank of the jet there are strong, anomalous low-level easterlies that suppress the formation of ARs closer
316 to the tropics. The handful of genesis points near the Baja California Peninsula are associated with relatively weak

southwesterly low-level winds near the tropics. When the jet modes are negative, genesis locations are co-located where the jet is strong in the west and central Pacific - which again is significantly further equatorward compared to the positive jet mode. The low-level winds associated with the low pressure anomaly south of the high pressure polar ridge support AR formation in the central and east Pacific. The orientation and location of the jet and the low-level wind anomalies generate strong IVT ARs as AR genesis occurs in warmer and moister latitudes.

Landfalling ARs in all of the nodes tend to form along the core location of the upper-level jet. However, east Pacific ARs can also form along anomalous southerly or southwesterly low-level winds. The jet and low-level wind location can influence the intensity of IVT associated with the ARs; if the jet position is closer to warmer, moister latitudes near the tropics and subtropics, then higher IVT values will be associated with the ARs. The opposite is true if these features are at higher latitudes.

4 | CONCLUSIONS

This study objectively identified 9 unique synoptic patterns associated with landfalling atmospheric river genesis using a 3x3 order SOM. These patterns are largely organized with positive and negative ENSO modes (ENSO, PDO, PNA, NP) in opposite corners and positive and negative jet modes (AO, WPO, EPO) in the other opposite corners. These synoptic conditions have differing frequencies throughout the cool season and produce ARs at different frequencies when they do occur. The variety of synoptic conditions produce and support landfalling ARs with largely unique lifecycle characteristics. The positive ENSO mode ARs, as compared to the negative mode ARs, form farther west in the Pacific basin, last longer, travel further, move faster, and have more zonal trajectories for most of their lifecycle. These ARs also tend to produce more precipitation in northern California and Washington; the negative mode ARs tend to produce more precipitation in southern California and in the interior of the U.S. These results are supported by previous work examining AR lifecycle characteristics, genesis location, and trajectory pathways. Zhou et al. (2018) and Zhou and Kim (2019) found that ARs with genesis in the west Pacific have longer lifecycle durations and have higher associated IVT. One key difference between our results and Zhou and Kim (2019), is that we have determined that ARs that form in the east and west Pacific can be associated with a variety of synoptic patterns. Guan and Waliser (2019)'s work also determined ARs that form near the western boundary of ocean basins are longer lived and that faster AR speeds are achieved when AR trajectories are over the west and central Pacific basin. Ryoo et al. (2013)'s study revealed air parcel trajectories during La Niñas to originate in the eastern Pacific with northeastward movement while during El Niños, trajectories originate from the subtropical western Pacific and propagate zonally.

For the jet mode ARs, the duration and distance traveled does not vary strongly between positive and negative phases. However, the genesis latitude, average track latitude, and meridional displacement of ARs are strongly affected. AR velocity is also affected but to a lesser degree compared to the positive and negative ENSO modes. The positive phase jet mode ARs have more poleward genesis and average track latitudes, travel slower, and tend to have more zonal trajectories. These characteristics lead to the negative (positive) phase jet mode ARs being associated with stronger (weaker) IVT signatures at genesis and landfall. Accordingly, the positive phase jet mode ARs generally bring the least amount of precipitation to much of the west coast while the negative phase is associated with enhanced precipitation in northern California, Oregon, and Washington. Parts of southern California, and the southwest interior receive more precipitation when positive. For all nodes, the synoptic patterns that support AR trajectories closer to the moist tropics tend to produce higher precipitation. As in Guirguis et al. (2019), we find that these jet modes have a stronger influence on modulating AR precipitation than the ENSO modes.

We additionally examine the large-scale circulation associated with landfalling AR genesis in each node. The

position and strength of the upper-level jet has a close relationship with AR activity (Payne and Magnusdottir (2014)) and particularly, AR genesis in the west and central Pacific. In the east Pacific, AR activity and genesis can be tied to southerly or southwesterly low-level wind anomalies which may be related to Rossby wave breaking strengthening the low-level winds and thus allowing the enhanced transport of tropical moisture. Although Rossby wave breaking was not analyzed in this study, we note that the corner nodes (Node 1 and 7) are associated with more cyclonic Rossby wave breaking events (rather than anticyclonic Rossby wave breaking events) as El Niños and negative WPO are known to be associated with higher cyclonic breaks (Ryoo et al. (2013); Rivière (2010)). Nodes 3 and 9 are associated with higher anticyclonic breaking events as they are related to La Niñas and positive WPO.

We have shown here that the different synoptic patterns ARs form under are an effective way of understanding an AR's lifecycle characteristics and impacts. The results indicate, for instance, that all strong ARs are not tied to a single type of synoptic condition but rather are possible under a range of conditions (such as during both El Niño and La Niña). The same could be said of genesis and landfall location. Thus, compositing of AR events given some criteria such as IVT intensity (Payne and Magnusdottir (2014)) or genesis/landfall region (Zhou and Kim (2019); Neiman et al. (2008)), as has been done in previous studies, can actually mix a variety of synoptic conditions together. Here, with inspiration from the methods presented in Guirguis et al. (2019), we let the background synoptic conditions - not an AR characteristic or a particular climate mode - dictate our grouping of ARs and these groupings reveal their own unique AR characteristics. Instead of looking at landfalling synoptic conditions, we focus on the conditions at genesis. We combine this with track and landfall information from individual AR events to see how these genesis conditions determine the kind of AR that makes landfall in the western U.S.

With the synoptic patterns associated with AR genesis established, we discuss potential applications beyond basic understanding of the relationship between genesis conditions and AR characteristics. These results lay the groundwork for potential future directions and studies. For example, one potential study can utilize statistical downscaling to investigate whether these synoptic patterns can be used to determine the distribution and magnitude of wintertime AR precipitation. Given a winter season with different frequencies of each node's synoptic pattern, can we estimate how much and where AR precipitation will fall? Additionally, there are several possible directions in the area of subseasonal-to-seasonal (S2S) forecasting. As predictions of large-scale climate modes, such as ENSO, become more accurate and at much longer lead times, the phases of these modes can be exploited to gain understanding of the types of synoptic patterns that can result and thereby help estimate the wintertime precipitation. Previous studies have already found success with ARs using certain phases of MJO and QBO (Baggett et al. (2017)). Another S2S related direction is to investigate the preconditions associated with each node. Benedict et al. (2019) examined precursors to landfalling ARs and found robust patterns with important connections to ARs over a week prior to landfall. The synoptic conditions identified in their study show promising similarities to nodes identified here. Lastly, future climates can be examined. In a warming climate, how do the frequency of these synoptic conditions and the various climate modes change?

5 | APPENDIX

5.1 | SOM description and parameters

We briefly outline how a SOM is trained iteratively: Each node is a vector containing weights for each grid in our spatial domain. We initialize each node in the SOM by randomly sampling from our AR genesis geopotential height anomaly samples. We then begin randomly sampling our data and determine the node that has the minimum Euclidean distance from this sample. We adjust this minimum distance node, or the 'winning' node, to more closely match the

sample (depends on learning rate). In addition, we adjust the neighbors of the winning node (depends on learning rate and neighborhood radius and function). We choose the next random sample and repeat.

For this study a SOM of order 3x3 (9 total nodes) is trained on AR genesis day samples. We use standardized geopotential height anomalies at 500 hPa as our variable of interest and weight the grid points by grid cell area. The SOM order of 3x3 was chosen over other configurations as the smaller size is easier to interpret, the corners are consistent when using larger orders, and the quality of the map is not significantly reduced. The SOM is implemented with python based software called MiniSom (Vettigli, 2020). The node vectors are randomly initialized as it has been shown to perform best for non-linear datasets (Akinduko et al., 2016). We perform training in two rounds as suggested in Hewitson and Crane (2002), Gibson et al. (2017), and Jiang et al. (2015). Gibson et al. (2017) and Jiang et al. (2015) found that reducing the radius so that only the winning node is updated (which is equivalent to k-means (Bação et al., 2005)) for the 2nd round of training produced more realistic and distinct synoptic patterns. The first round is the ordering phase with a large neighborhood radius and learning rate which allows the map's structure to develop. The second round is the convergent phase with a smaller radius and learning rate where the finer details can develop. During the first phase, the initial neighborhood radius and learning rate decay exponentially and run through 51350 (50x the sample size of 1027 ARs) iterations total. The second phase holds the radius constant so only the winning node will be updated. The learning rate also decays in this second phase and runs through 51350 iterations. The decay function used in MiniSom is:

$$val\_t = \frac{val\_0}{1 + \frac{t}{\left(\frac{max\_iter}{2}\right)}}, \tag{2}$$

where val_t is the value of the neighborhood radius or learning rate at iteration t, val_0 is either the initial radius or learning rate, t is the current iteration, and max_iter is the total number of iterations in a training phase. We use an initial radius of 2 (1) and a learning rate of 0.1 (0.05) during the ordering phase (convergent phase). After training the SOM, each AR event is classified into one of the nine nodes based on best match as determined by Euclidean distance of gridded features between genesis day and SOM node; this winning node is sometimes referred to as the "best matching unit" (BMU). We then create composites for each node based on all of the genesis days of the AR events associated with that node.

5.2 | Differences in GW19

We perform SOM and AR characteristic analysis on the GW19 dataset. GW19, similar to the Mundhenk algorithm, catalogues ARs globally using a relative threshold on IVT along with additional geometric criteria. It tracks all ARs regardless of the AR making landfall or not and includes ARs making landfall outside of the U.S. west coast (California to Washington). In ARTMIP (Rutz et al. (2019)), relative methods were found to perform quite similarly although the Guan algorithm is more permissive. The Guan algorithm is an outlier over polar regions and inland areas due to its low relative IVT percentile threshold at 85%.

We include this analysis to examine how a purely landfalling AR dataset compares to a dataset that considers all ARs - landfalling or not. We do not perform landfalling analysis on this dataset as the location and date of landfalling can be ambiguous for a given event. The ambiguity comes from the catalogue allowing the same AR to make landfall more than once, at various locations, across several timesteps. We subset the global catalogue for ARs with genesis in the North Pacific domain of 10N-52.5N,110E-250E. The total number events associated with the total for the Guan and Waliser dataset is 2806.

To reiterate, the two key differences between the GW19 dataset and the Gonzales dataset are that the GW19 dataset considers all ARs, landfalling and non-landfalling, and considers all North Pacific ARs, regardless of where they make landfall (as opposed to strictly U.S. west coast landfalling ARs).

We now discuss differences between the SOMs trained on the Gonzales and GW19 AR catalogues. Nodes 3, 5, and 7 show the most differences. Node 3's synoptic conditions in the Gonzales SOM supports moisture transport along a poleward tilted jet with a coastal low-level wind anomaly bringing moisture to the U.S. west coast. In contrast, Node 3's synoptic conditions in the GW19 SOM are more favorable for moisture transport to Canada and Alaska in particular but also to the Baja California Peninsula and features a slightly less eastward extended jet (Fig. S8 and Fig. S6). While both feature high pressure anomalies throughout the North Pacific basin, for ARs to make landfall on the U.S. west coast, the high pressure anomaly in the eastern Pacific needs to remain at lower latitudes otherwise the moisture will be transported north of the U.S. western states. Because the high pressure in the GW19 SOM reaches higher latitudes near Alaska, the positive EPO mean in the Gonzales SOM for Node 3 turns to a negative mean for EPO. It is one of 3 node and climate index pairs in all of the nodes and indices considered that changes phase (the NP (AO) Node 2 (Node 5) is slightly positive (negative) with the Gonzales data and becomes slightly negative (positive) in GW19).

For Node 5, the Gonzales synoptic conditions, in particular, favor a more eastward extended jet due to the low geopotential height anomaly in the central North Pacific compared to the high anomaly in the GW19 synoptic conditions.

The GW19 Node 7 synoptic conditions favor moisture transport to Canada as opposed to the Gonzales synoptic conditions which favor transport to Oregon and Washington (seen most clearly in the low-level winds shown in Fig. S7 and Fig. S8). Both feature a low geopotential height anomaly in the central North Pacific but have differing locations for the high latitude ridge - the GW19 positive height anomalies are over the Pacific northwest while the Gonzales height anomalies are stronger and over Siberia and Alaska.

Next, we compare the lifecycle characteristics. As with the Gonzales dataset, significance is implied using a t-test for unequal means at 95% confidence unless specifically stated otherwise. In the GW19 SOM, the positive ENSO node (Node 1) has, on average, AR genesis occurring $>10°$ more east, longer AR durations (7.4 hrs; not signficantly different at 95% confidence but significant at 90% confidence), travel farther distances (963 km), faster velocities (6.4 km/hr), and the most stark contrast in the ratio between zonal and meridional displacement throughout the AR lifecycle compared to the negative ENSO node (Node 9). These characteristics are largely consistent with the Gonzales dataset although the contrast between the nodes is not as strong (e.g. Node 1 vs Node 9 durations in GW19 is 7.4 hr difference compared to the over 24 hr difference in the Gonzales dataset). As for the jet modes, both genesis latitude (1°; significant at 90% confidence) and average latitude (1.9°) are further north for the positive node (Node 3) compared to the negative node (Node 7) which is also consistent with the Gonzales dataset. AR velocities are slightly faster in the negative mode by 3.3 km/hr (significant at 90%). The negative mode also exhibits more meridional displacement (significant at 90% confidence). Again, the differences here are not as strong compared to the Gonzales dataset between positive and negative jet modes.

The differences in the synoptic patterns and characteristics reflect the differences in these two AR catalogues; the Gonzales dataset is strictly U.S. west coast landfalling ARs while the GW19 dataset considers all North Pacific ARs regardless of if they make landfall or make landfall in regions outside of the U.S. west coast. Thus, the Gonzales synoptic patterns support moisture transport targeting the U.S. west coast while the GW19 synoptic patterns may support moisture transport to higher latitudes such as Canada for instance. With the AR characteristics, the differences are not as strong between the positive and negative modes due a wider variety of ARs being included with each node - not just landfalling ARs.

Acknowledgements

SK was supported by the Geography Department at the University of California, Berkeley. We acknowledge NERSC for the allocation of computational resources which enabled us to perform the data analysis. We thank and acknowledge Bin Guan for providing the Guan and Waliser (2019) dataset. Lastly, we sincerely thank 3 anonymous reviewers for carefully reading the manuscript and for providing suggestions which have improved and clarified the manuscript.

Conflict of Interest

The authors declare that there is no conflict of interest regarding the publication of this paper.

References

Akinduko, A. A., Mirkes, E. M. and Gorban, A. N. (2016) Som: Stochastic initialization versus principal components. *Information Sciences*, **364**, 213–221.

Bação, F., Lobo, V. and Painho, M. (2005) Self-organizing maps as substitutes for k-means clustering. In *International Conference on Computational Science*, 476–483. Springer.

Baggett, C. F., Barnes, E. A., Maloney, E. D. and Mundhenk, B. D. (2017) Advancing atmospheric river forecasts into subseasonal-to-seasonal time scales. *Geophysical Research Letters*, **44**, 7528–7536.

Bao, J., Michelson, S., Neiman, P., Ralph, F. and Wilczak, J. (2006) Interpretation of enhanced integrated water vapor bands associated with extratropical cyclones: Their formation and connection to tropical moisture. *Monthly weather review*, **134**, 1063–1080.

Benedict, J. J., Clement, A. C. and Medeiros, B. (2019) Atmospheric blocking and other large-scale precursor patterns of landfalling atmospheric rivers in the north pacific: A cesm2 study. *Journal of Geophysical Research: Atmospheres*, **124**, 11330–11353.

Dettinger, M. D., Ralph, F. M., Das, T., Neiman, P. J. and Cayan, D. R. (2011) Atmospheric rivers, floods and the water resources of california. *Water*, **3**, 445–478.

Florsheim, J. L. and Dettinger, M. D. (2015) Promoting atmospheric-river and snowmelt-fueled biogeomorphic processes by restoring river-floodplain connectivity in california's central valley. In *Geomorphic approaches to integrated floodplain management of lowland fluvial systems in North America and Europe*, 119–141. Springer.

Gelaro, R., McCarty, W., Suárez, M. J., Todling, R., Molod, A., Takacs, L., Randles, C. A., Darmenov, A., Bosilovich, M. G., Reichle, R. et al. (2017) The modern-era retrospective analysis for research and applications, version 2 (merra-2). *Journal of Climate*, **30**, 5419–5454.

Gibson, P. B., Perkins-Kirkpatrick, S. E., Uotila, P., Pepler, A. S. and Alexander, L. V. (2017) On the use of self-organizing maps for studying climate extremes. *Journal of Geophysical Research: Atmospheres*, **122**, 3891–3903.

Gimeno, L., Nieto, R., Vázquez, M. and Lavers, D. A. (2014) Atmospheric rivers: A mini-review. *Frontiers in Earth Science*, **2**, 2.

Gonzales, K. R., Swain, D. L., Nardi, K. M., Barnes, E. A. and Diffenbaugh, N. S. (2019) Recent warming of landfalling atmospheric rivers along the west coast of the united states. *Journal of Geophysical Research: Atmospheres*, **124**, 6810–6826.

Guan, B. and Waliser, D. E. (2015) Detection of atmospheric rivers: Evaluation and application of an algorithm for global studies. *Journal of Geophysical Research: Atmospheres*, **120**, 12514–12535.

— (2019) Tracking atmospheric rivers globally: Spatial distributions and temporal evolution of life cycle characteristics. *Journal of Geophysical Research: Atmospheres*.

Guirguis, K., Gershunov, A., Shulgina, T., Clemesha, R. E. and Ralph, F. M. (2019) Atmospheric rivers impacting northern california and their modulation by a variable climate. *Climate dynamics*, **52**, 6569–6583.

Hecht, C. W. and Cordeira, J. M. (2017) Characterizing the influence of atmospheric river orientation and intensity on precipitation distributions over north coastal california. *Geophysical Research Letters*, **44**, 9048–9058.

Hewitson, B. and Crane, R. G. (2002) Self-organizing maps: applications to synoptic climatology. *Climate Research*, **22**, 13–26.

Hu, H., Dominguez, F., Wang, Z., Lavers, D. A., Zhang, G. and Ralph, F. M. (2017) Linking atmospheric river hydrological impacts on the us west coast to rossby wave breaking. *Journal of Climate*, **30**, 3381–3399.

Hughes, M., Mahoney, K. M., Neiman, P. J., Moore, B. J., Alexander, M. and Ralph, F. M. (2014) The landfall and inland penetration of a flood-producing atmospheric river in arizona. part ii: Sensitivity of modeled precipitation to terrain height and atmospheric river orientation. *Journal of Hydrometeorology*, **15**, 1954–1974.

Jiang, N., Luo, K., Beggs, P. J., Cheung, K. and Scorgie, Y. (2015) Insights into the implementation of synoptic weather-type classification using self-organizing maps: an australian case study. *International Journal of Climatology*, **35**, 3471–3485.

JISAO (2020) Pacific decadal oscillation (pdo) index. `http://research.jisao.washington.edu/data_sets/pdo/#analysis`.

Kohonen, T. (1982a) Self-organized formation of topologically correct feature maps. *Biological cybernetics*, **43**, 59–69.

— (1982b) A simple paradigm for the self-organized formation of structured feature maps. In *Competition and cooperation in neural nets*, 248–266. Springer.

Kohonen, T., Schroeder, M. R. and Huang, T. S. (2001) *Self-Organizing Maps*. Berlin, Heidelberg: Springer-Verlag, 3rd edn.

Liu, Y. and Weisberg, R. H. (2011) A review of self-organizing map applications in meteorology and oceanography. *Self-Organizing Maps: Applications and Novel Algorithm Design*, 253–272.

Mundhenk, B. D., Barnes, E. A. and Maloney, E. D. (2016) All-season climatology and variability of atmospheric river frequencies over the north pacific. *Journal of Climate*, **29**, 4885–4903.

Neiman, P. J., Ralph, F. M., Moore, B. J., Hughes, M., Mahoney, K. M., Cordeira, J. M. and Dettinger, M. D. (2013) The landfall and inland penetration of a flood-producing atmospheric river in arizona. part i: Observed synoptic-scale, orographic, and hydrometeorological characteristics. *Journal of Hydrometeorology*, **14**, 460–484.

Neiman, P. J., Ralph, F. M., Wick, G. A., Lundquist, J. D. and Dettinger, M. D. (2008) Meteorological characteristics and overland precipitation impacts of atmospheric rivers affecting the west coast of north america based on eight years of ssm/i satellite observations. *Journal of Hydrometeorology*, **9**, 22–47.

Neiman, P. J., Schick, L. J., Ralph, F. M., Hughes, M. and Wick, G. A. (2011) Flooding in western washington: The connection to atmospheric rivers. *Journal of Hydrometeorology*, **12**, 1337–1358.

NOAA (2020a) Climate indices ftp. `https://ftp.cpc.ncep.noaa.gov/cwlinks/`.

— (2020b) Climate prediction center (cpc) oceanic nino index. `https://catalog.data.gov/dataset/climate-prediction-center-cpcoceanic-nino-index/resource/76d3775a-3fff-48f9-aa6a-c1d084bcefbe`.

— (2020c) Daily climate timeseries: Epo. `https://www.esrl.noaa.gov/psd/data/timeseries/daily/EPO/`.

— (2020d) Daily climate timeseries: Wpo. `https://www.esrl.noaa.gov/psd/data/timeseries/daily/WPO/`.

Payne, A. E. and Magnusdottir, G. (2014) Dynamics of landfalling atmospheric rivers over the north pacific in 30 years of merra reanalysis. *Journal of Climate*, **27**, 7133–7150.

Radić, V., Cannon, A. J., Menounos, B. and Gi, N. (2015) Future changes in autumn atmospheric river events in british columbia, canada, as projected by cmip5 global climate models. *Journal of Geophysical Research: Atmospheres*, **120**, 9279–9302.

552 Ralph, F. and Dettinger, M. (2011) Storms, floods, and the science of atmospheric rivers. *Eos, Transactions American Geophysical*
553   *Union*, **92**, 265–266.

554 Ralph, F. M., Dettinger, M., Lavers, D., Gorodetskaya, I. V., Martin, A., Viale, M., White, A. B., Oakley, N., Rutz, J., Spackman, J. R.
555   et al. (2017) Atmospheric rivers emerge as a global science and applications focus. *Bulletin of the American Meteorological*
556   *Society*, **98**, 1969–1973.

557 Ralph, F. M., Neiman, P. J., Wick, G. A., Gutman, S. I., Dettinger, M. D., Cayan, D. R. and White, A. B. (2006) Flooding on
558   california's russian river: Role of atmospheric rivers. *Geophysical Research Letters*, **33**.

559 Ralph, F. M., Rutz, J. J., Cordeira, J. M., Dettinger, M., Anderson, M., Reynolds, D., Schick, L. J. and Smallcomb, C. (2019) A
560   scale to characterize the strength and impacts of atmospheric rivers. *Bulletin of the American Meteorological Society*, **100**,
561   269–289.

562 Rivière, G. (2010) Role of rossby wave breaking in the west pacific teleconnection. *Geophysical research letters*, **37**.

563 Rutz, J. J., Shields, C. A., Lora, J. M., Payne, A. E., Guan, B., Ullrich, P., O'Brien, T., Leung, L. R., Ralph, F. M., Wehner, M. et al.
564   (2019) The atmospheric river tracking method intercomparison project (artmip): Quantifying uncertainties in atmospheric
565   river climatology. *Journal of Geophysical Research: Atmospheres*.

566 Rutz, J. J., Steenburgh, W. J. and Ralph, F. M. (2014) Climatological characteristics of atmospheric rivers and their inland
567   penetration over the western united states. *Monthly Weather Review*, **142**, 905–921.

568 Ryoo, J.-M., Kaspi, Y., Waugh, D. W., Kiladis, G. N., Waliser, D. E., Fetzer, E. J. and Kim, J. (2013) Impact of rossby wave breaking
569   on us west coast winter precipitation during enso events. *Journal of Climate*, **26**, 6360–6382.

570 Ryoo, J.-M., Waliser, D. E., Waugh, D. W., Wong, S., Fetzer, E. J. and Fung, I. (2015) Classification of atmospheric river events
571   on the us west coast using a trajectory model. *Journal of Geophysical Research: Atmospheres*, **120**, 3007–3028.

572 Schlef, K. E., Moradkhani, H. and Lall, U. (2019) Atmospheric circulation patterns associated with extreme united states floods
573   identified via machine learning. *Scientific reports*, **9**, 1–12.

574 Sellars, S., Kawzenuk, B., Nguyen, P., Ralph, F. and Sorooshian, S. (2017) Genesis, pathways, and terminations of intense global
575   water vapor transport in association with large-scale climate patterns. *Geophysical Research Letters*, **44**, 12–465.

576 Sheridan, S. C. and Lee, C. C. (2011) The self-organizing map in synoptic climatological research. *Progress in Physical Geography*,
577   **35**, 109–119.

578 Shields, C. A., Rutz, J. J., Leung, L.-Y., Ralph, F. M., Wehner, M., Kawzenuk, B., Lora, J. M., McClenny, E., Osborne, T., Payne,
579   A. E., Ullrich, P., Gershunov, A., Goldenson, N., Guan, B., Qian, Y., Ramos, A. M., Sarangi, C., Sellars, S., Gorodetskaya, I.,
580   Kashinath, K., Kurlin, V., Mahoney, K., Muszynski, G., Pierce, R., Subramanian, A. C., Tome, R., Waliser, D., Walton, D.,
581   Wick, G., Wilson, A., Lavers, D., Prabhat, Collow, A., Krishnan, H., Magnusdottir, G. and Nguyen, P. (2018) Atmospheric
582   river tracking method intercomparison project (ARTMIP): project goals and experimental design. *Geoscientific Model De-*
583   *velopment*, **11**, 2455–2474. URL: `https://www.geosci-model-dev.net/11/2455/2018/`.

584 Skific, N. and Francis, J. (2012) Self-organizing maps: a powerful tool for the atmospheric sciences. *Applications of Self-*
585   *Organizing Maps*, 251–268.

586 Swales, D., Alexander, M. and Hughes, M. (2016) Examining moisture pathways and extreme precipitation in the us inter-
587   mountain west using self-organizing maps. *Geophysical Research Letters*, **43**, 1727–1735.

588 UCAR (2020) North pacific (np) index. `https://climatedataguide.ucar.edu/climate-data/north-pacific-np-index-`
589   `trenberth-and-hurrell-monthly-and-winter`.

590 Vettigli, G. (2020) Minisom. `https://github.com/JustGlowing/minisom`. [Online; accessed 26-March-2020].

Waliser, D. and Guan, B. (2017) Extreme winds and precipitation during landfall of atmospheric rivers. *Nature Geoscience*, **10**, 179–183.

Zhang, W. and Villarini, G. (2018) Uncovering the role of the east asian jet stream and heterogeneities in atmospheric rivers affecting the western united states. *Proceedings of the National Academy of Sciences*, **115**, 891–896.

Zhou, Y. and Kim, H. (2019) Impact of distinct origin locations on the life cycles of landfalling atmospheric rivers over the us west coast. *Journal of Geophysical Research: Atmospheres*, **124**, 11897–11909.

Zhou, Y., Kim, H. and Guan, B. (2018) Life cycle of atmospheric rivers: Identification and climatological characteristics. *Journal of Geophysical Research: Atmospheres*, **123**, 12–715.

Zhu, Y. and Newell, R. E. (1998) A proposed algorithm for moisture fluxes from atmospheric rivers. *Monthly weather review*, **126**, 725–735.
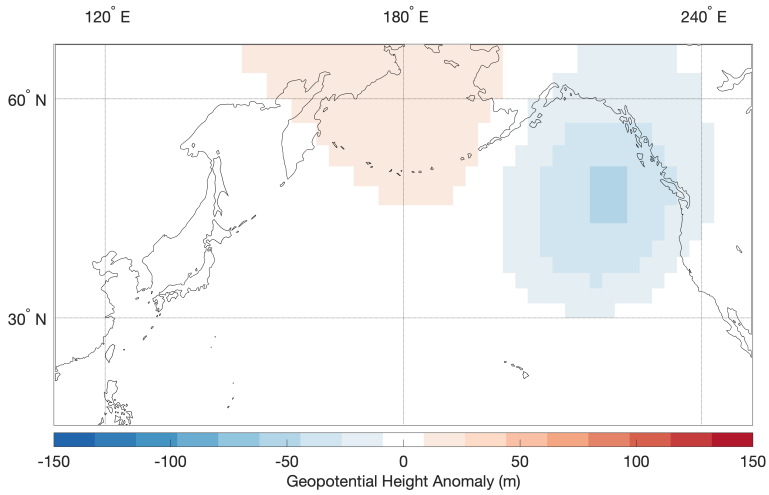
FIGURE 1 Composite of 500 hPa geopotential height anomalies occurring on the genesis day of all U.S. west coast landfalling ARs (November - February, 1980-2015).

Climate Index	Temporal Resolution	Data Source
ONI	*monthly*	NOAA (2020b)
PDO	*monthly*	JISAO (2020)
NP	*monthly*	UCAR (2020)
PNA	*daily*	NOAA (2020a)
AO	*daily*	NOAA (2020a)
WPO	*daily*	NOAA (2020d)
EPO	*daily*	NOAA (2020c)

TABLE 1 Climate indices evaluated with the SOM along with their temporal resolution and data source.
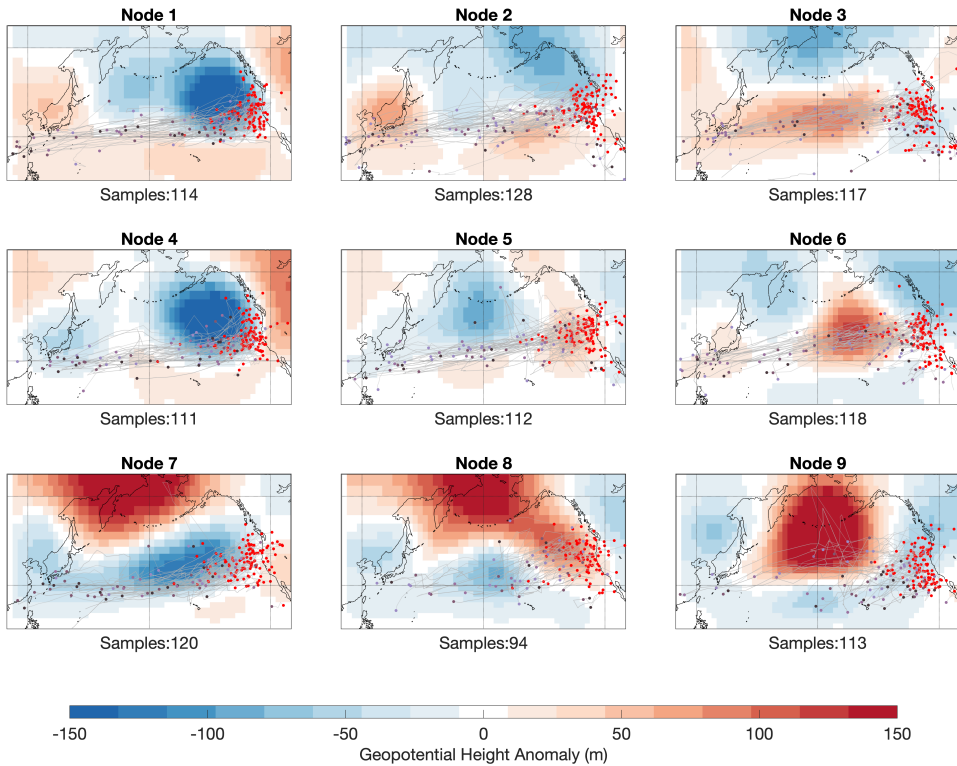
FIGURE 2 The SOM trained on AR genesis day 500 hPa geopotential height anomalies. The nodes are composites of the genesis day geopotential heights of all the ARs that are assigned to a given node. The AR tracks are also displayed with the genesis points in purple and the landfall points in red. The landfall points do not fall precisely on the coast because the track points represent the IVT weighted centroid of the AR object at a given timestep. Thus, when a zonally long AR's leading edge makes landfall, the IVT weighted centroid may be located far off coast.
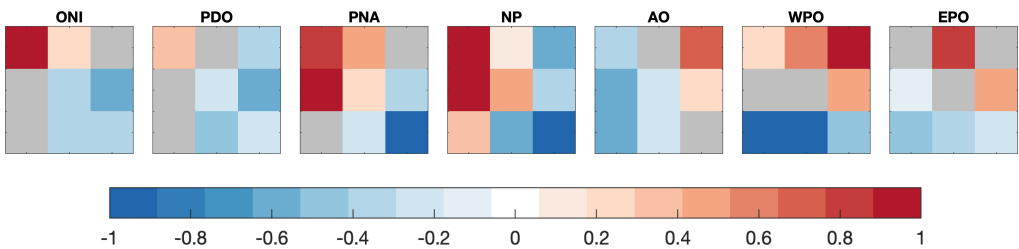
FIGURE 3 The various climate indices' average values for each node corresponding with the SOM in Fig. 2. The averages were calculated from the value of the index on all the AR genesis days associated with a node. Red (blue) values indicate positive (negative) phases of the respective indices. White values indicate neutral conditions or not statistically different from climatology (t-test for unequal means, 90% confidence).

(a)   (b)
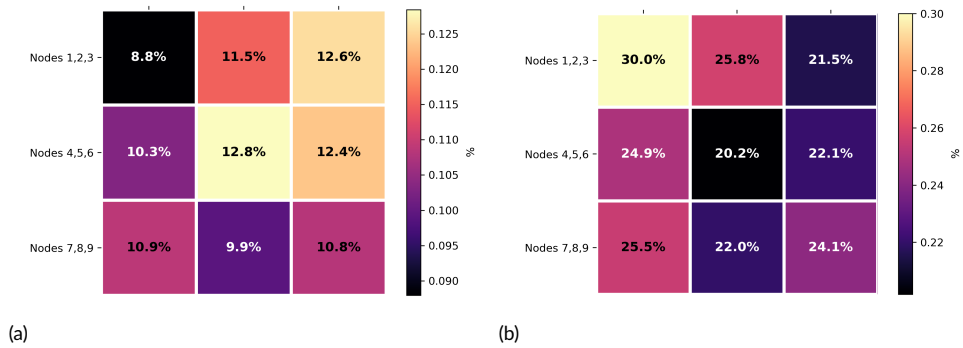
FIGURE 4   a) Percentage of all cool season (Nov-Feb) days that best match the synoptic conditions of each node. b) Percentage of AR genesis days occurring during the cool season days that match the synoptic conditions of each node.

Node #	Genesis	Landfall	Dur (hr)	Dist (km)	Vel (km/hr)	Lat	Lon	Merid	Zonal	Aspect
1	32.3N,177.0E	39.2N,228.7E	103.8	7413	67.3	34.3N	196.6E	6.9	51.7	7.5
2	32.4N,175.3E	40.8N,230.0E	99.3	6627	65.8	36.2N	192.5E	8.4	54.7	6.5
3	32.4N,182.6E	39.0N,230.6E	92.2	5720	59.2	36.2N	195.6E	6.6	48.0	7.3
4	32.9N,185.8E	39.7N,228.6E	85.4	5892	70.2	34.7N	199.1E	6.7	42.9	6.4
5	33.7N,176.8E	40.6N,229.3E	97.6	6718	67.7	36.3N	195.8E	7.0	52.5	7.5
6	32.8N,181.5E	39.8N,229.8E	66.4	6012	68.1	36.9N	195.3E	6.9	48.4	7.0
7	30.4N,179.0E	39.4N,227.6E	98.4	6226	64.7	33.3N	197.8E	9.1	48.6	5.3
8	33.7N,191.3E	40.7N,229.5E	83.7	5098	62.2	35.9N	202.3E	6.9	38.2	5.5
9	31.1N,199.1E	37.3N,230.9E	77.2	4430	55.2	35.2N	206.0E	6.2	31.9	5.1

TABLE 2 Summary of various AR characteristics associated with each node of the SOM: genesis coordinate (Col 2), landfall coordinate (Col 3), AR lifecycle duration in hrs (Col 4), distance traveled in km (Col 5), average velocity in km/hr (Col 6), AR track latitude (Col 7), AR track longitude (Col 8), AR meridional movement in degrees (Col 9), AR zonal movement in degrees (Col 10), and the ratio between zonal movement and meridional movement (Col 11).
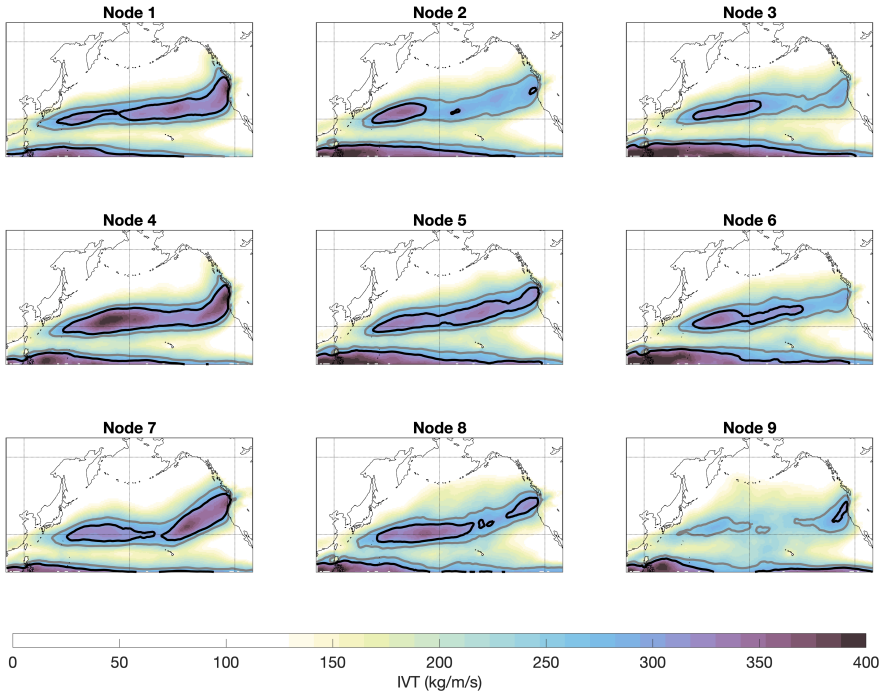
FIGURE 5 Composites of IVT on the landfall day of all the ARs associated with each node of the SOM. Light gray (black) contour at 250 (300) kg/m/s.
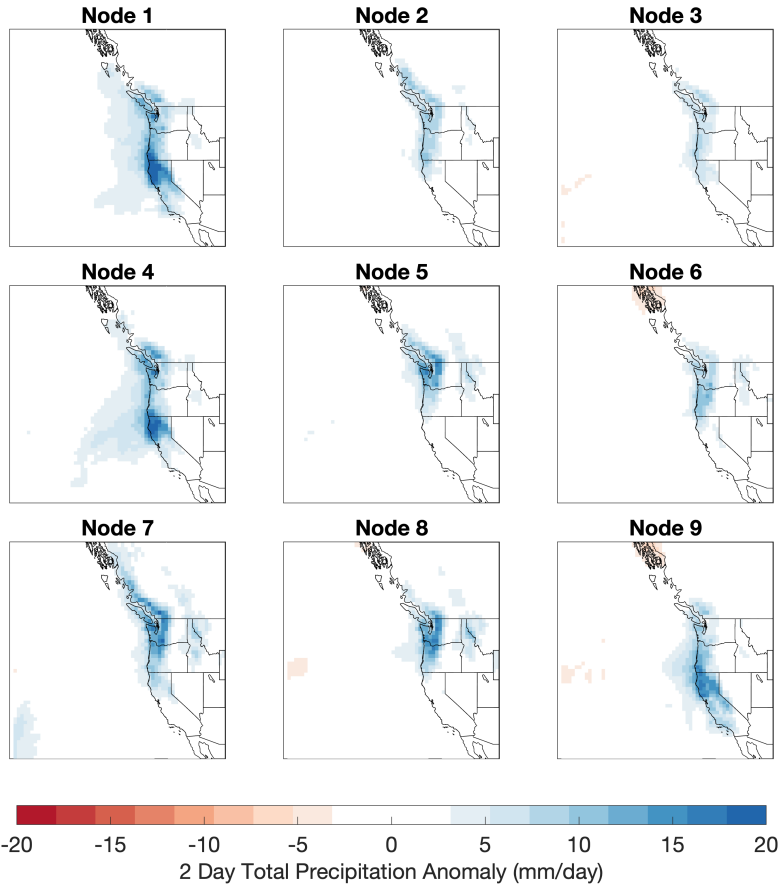
FIGURE 6 Composites of precipitation anomaly over 2 days (landfall day and the following day) of all the ARs associated with each node of the SOM.
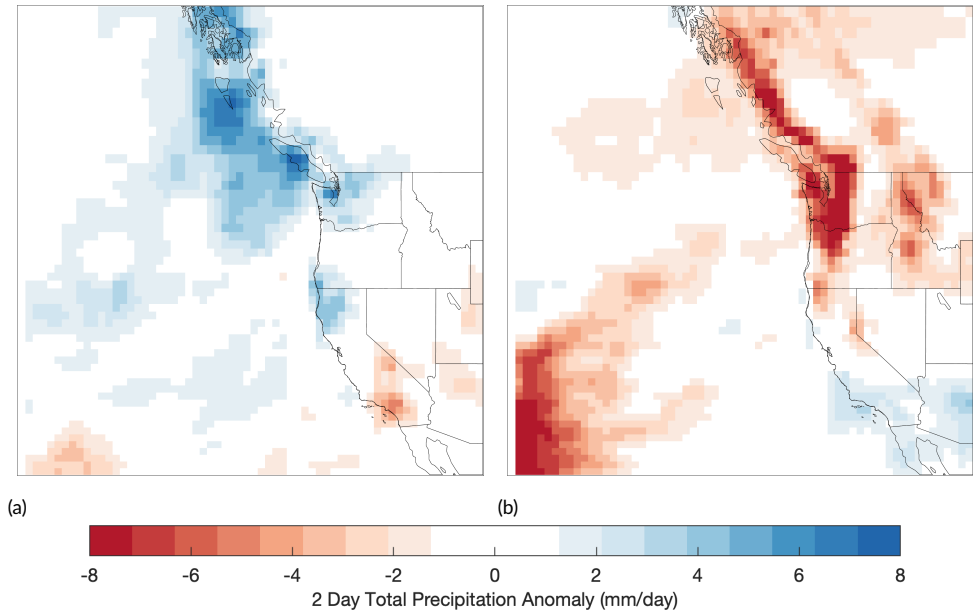
(a)   (b)

FIGURE 7 Precipitation anomaly over 2 days on and the following day of landfall. a) Positive phase node (Node 1) of the ENSO modes minus the negative phase node (Node 9). b) Positive phase node (Node 3) of the jet modes minus the negative phase node (Node 7).
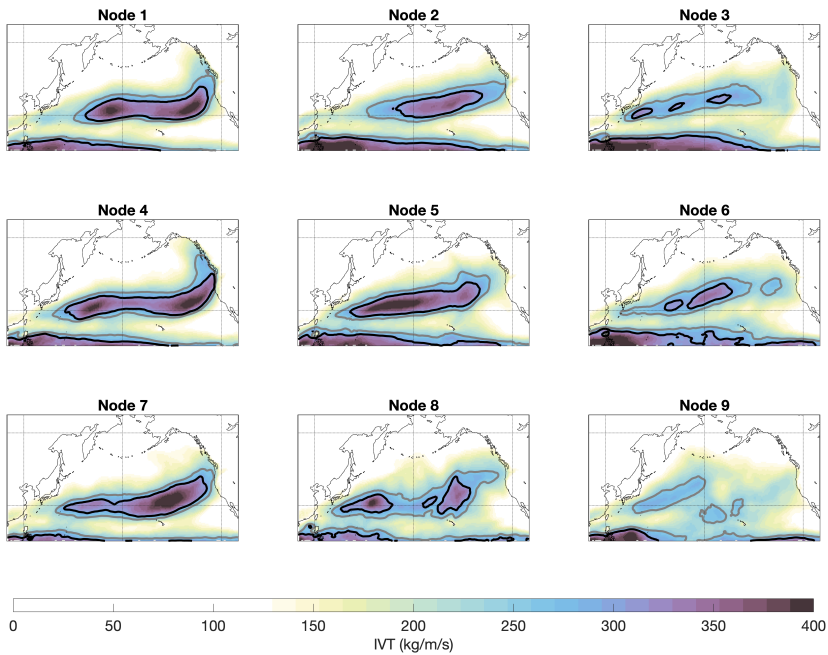
FIGURE 8 Composites of IVT on genesis day. Light gray (black) contour at 250 (300) kg/m/s.
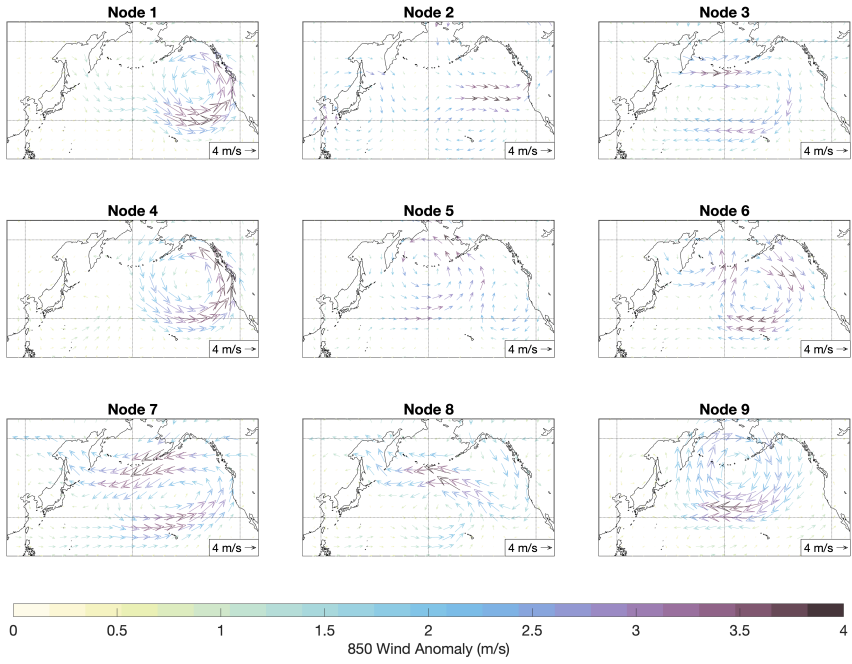
FIGURE 9 Composites of the 850 hPa wind anomaly on genesis day.
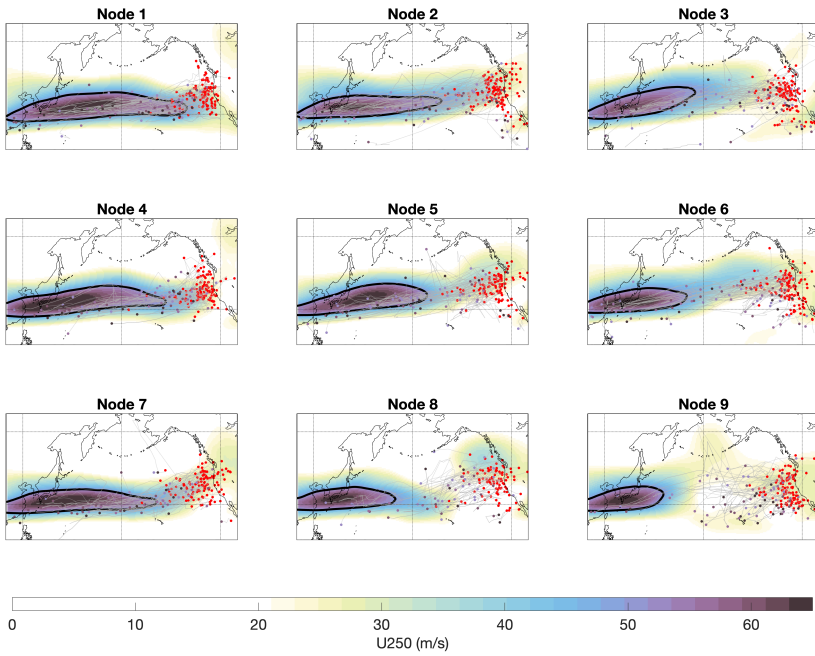
FIGURE 10 Composites of the 250 hPa zonal wind on genesis day. AR track information (same as Fig. 2) is overlaid. Black contour at 50 m/s.
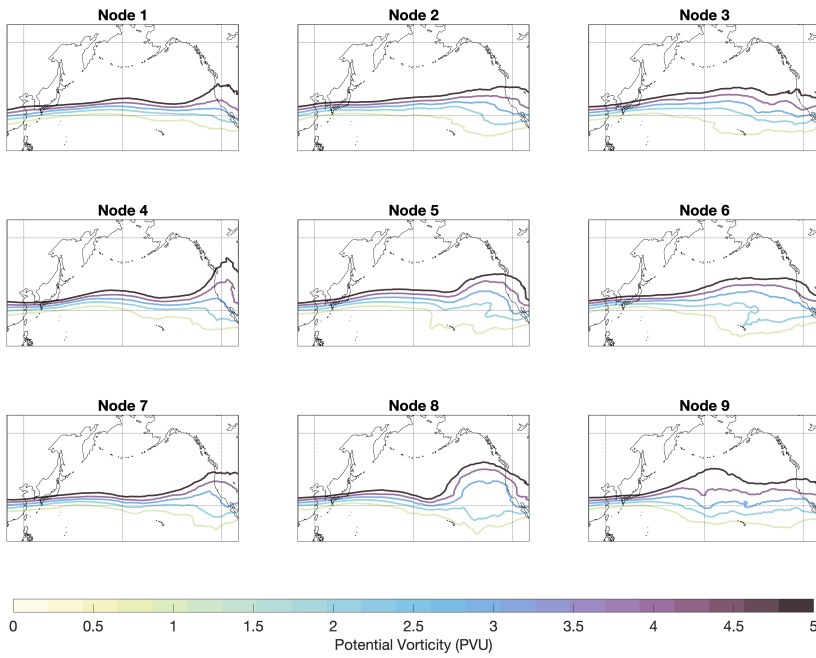
FIGURE 11   Composites of upper-level (200 hPa) PV on AR genesis day.

6 | SUPPORTING INFORMATION
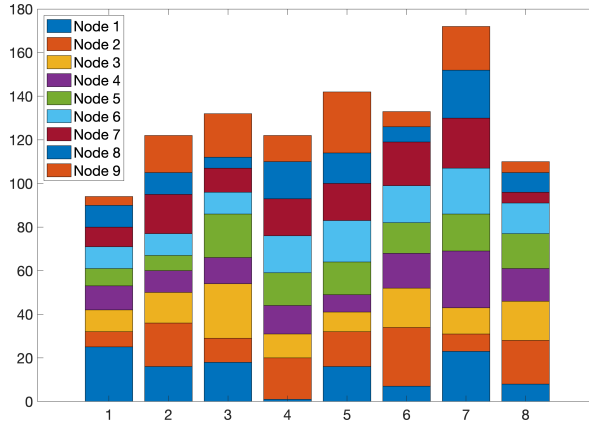
FIGURE S1 MJO phase frequency distributions for AR genesis days from the Gonzalez catalogue. Each bar is stacked with 9 colors representing the contributions from each of the 9 nodes with node 1 at the bottom and node 9 at the top. Landfalling U.S. AR genesis is most frequent during Phase 7 of the MJO and is the least frequent during Phase 1 of the MJO.
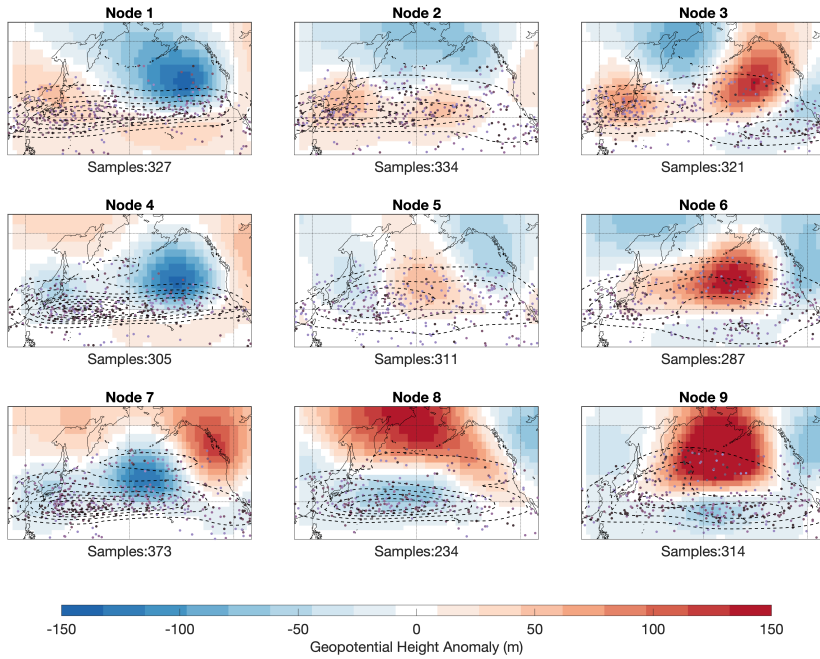
FIGURE S2 Same as in Fig. 2 but trained on the Guan and Waliser catalogue which contains all ARs (landfalling and non-landfalling) in the North Pacific. Termination points and tracks are excluded. Instead, probability density estimate contours of genesis points are included. Contours levels are at 0.00015.
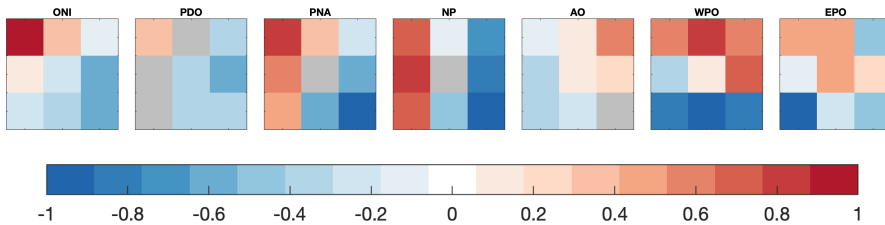
FIGURE S3 Same as in Fig. 3 but corresponding with the SOM in Fig. S2.

Node #	Genesis	Landfall	Dur (hr)	Dist (km)	Vel (km/hr)	Lat	Lon	Merid	Zonal	Aspect
1	31.6N,171.2E	NA	69.4	4852	67.3	35.9N	194.3E	8.7	36.4	4.2
2	32.5N,175.2E	NA	69.4	4689	64.5	38.1N	196.5E	9.6	35.2	3.7
3	31.4N,177.4E	NA	69.3	4680	64.3	38.1N	199.3E	10.5	26.6	2.5
4	31.2N,173.3E	NA	69.8	4812	69.0	35.8N	196.4E	9.2	32.9	3.6
5	31.9N,181.4E	NA	62.2	4188	65.4	38.1N	199.3E	8.4	28.4	3.4
6	32.1N,181.7E	NA	59.3	3927	63.8	37.5N	196.9E	7.4	22.4	3.0
7	30.4N,175.6E	NA	70.7	5008	67.6	36.2N	196.0E	11.1	31.8	2.8
8	32.0N,174.6E	NA	69.4	4515	64.3	36.9N	196.6E	10.4	28.7	2.8
9	31.6N,182.0E	NA	62.0	3889	60.9	37.6N	197.7E	9.5	14.3	1.5

TABLE S1 Same as Table 2 but for the GW19 dataset.
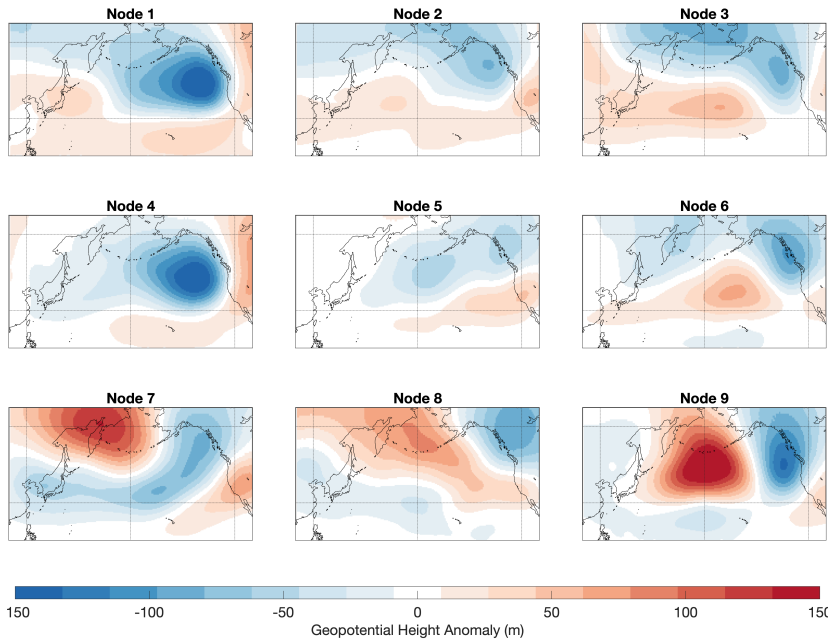
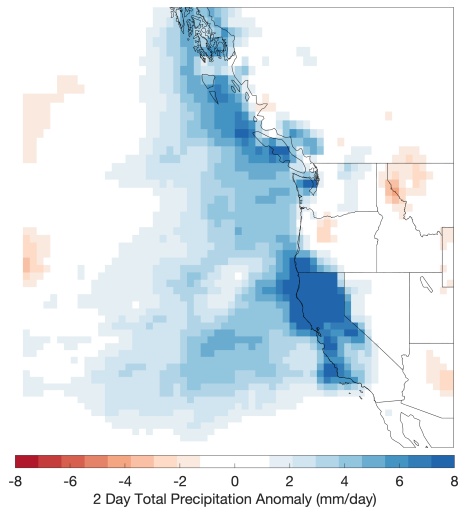**FIGURE S4** Landfalling 500 hPa geopotential height anomalies.

FIGURE S5 Precipitation anomaly over 2 days on and the following day of landfall. Anomaly differences for the most El Niño node (Node 1) and the most La Niña node (Node 6).
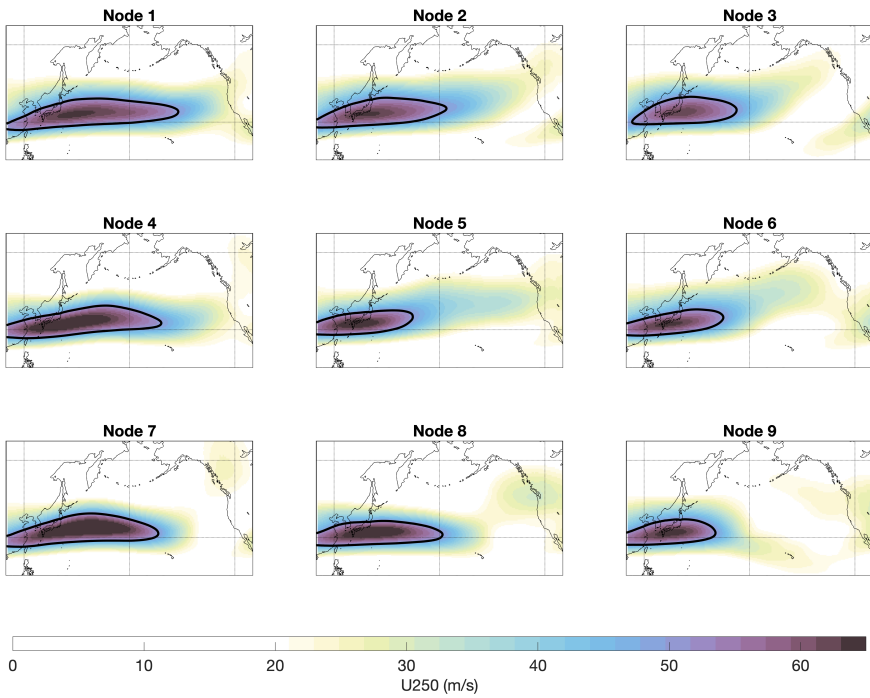
FIGURE S6 Composites of the 250 hPa zonal wind on genesis day for the GW19 dataset. Black contour at 50 m/s.
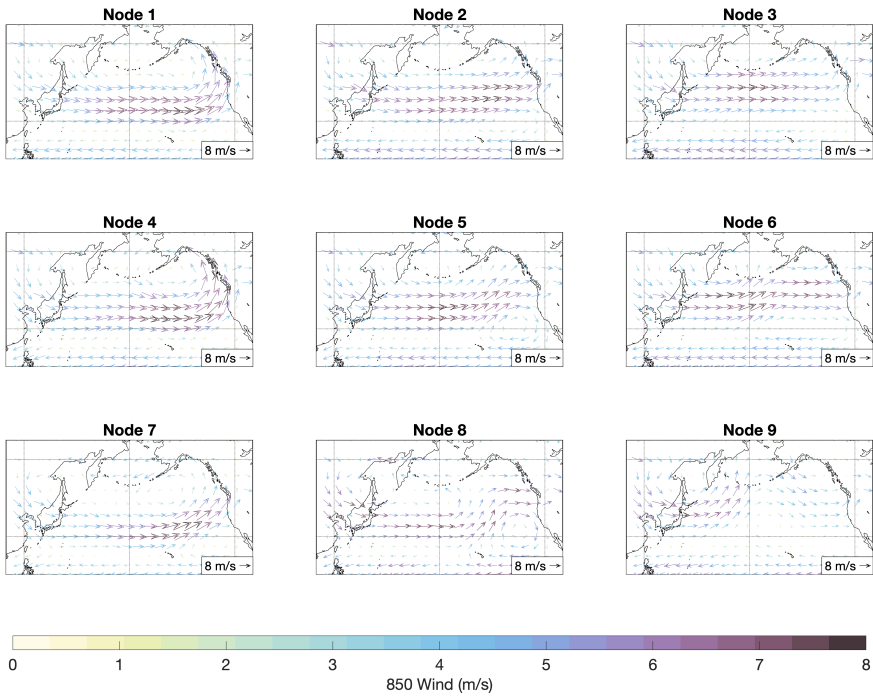
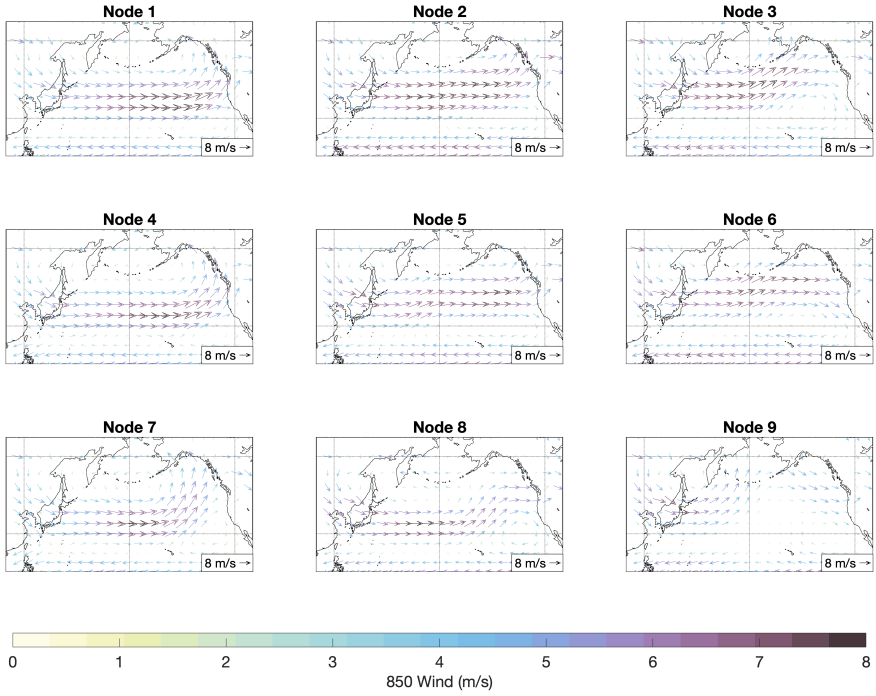**FIGURE S7** Composites of the 850 hPa wind on genesis day (not anomalies).

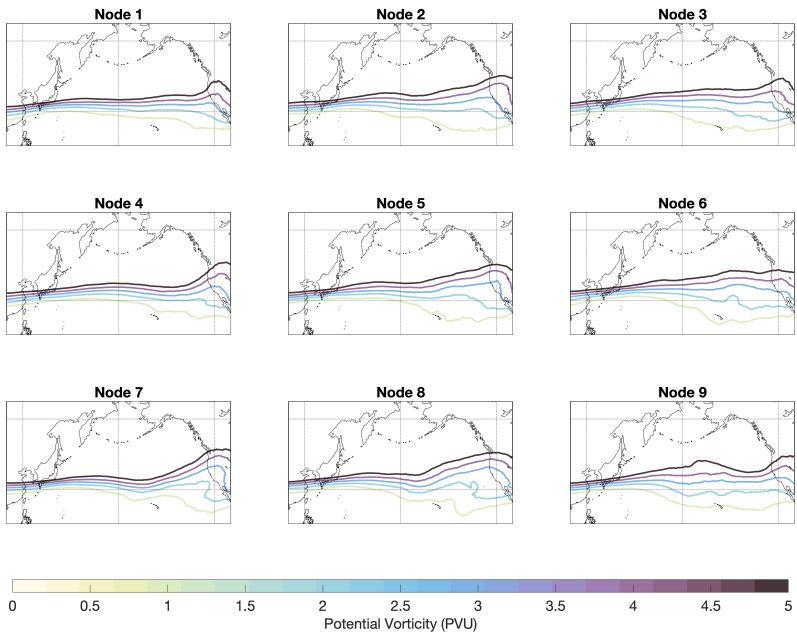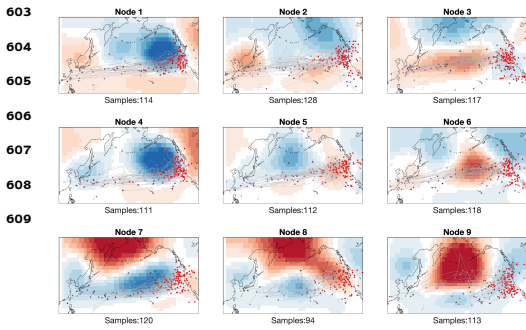**FIGURE S8** Same as Fig. S7 but for the GW19 dataset.

FIGURE S9 Composites of upper-level (200 hPa) PV on AR landfall day.

GRAPHICAL ABSTRACT

The range of synoptic patterns that North Pacific landfalling atmospheric rivers form under are objectively identified using genesis day 500 hPa geopotential height anomalies in a self-organizing map. The nine identified synoptic patterns produce ARs with distinct lifecycle characteristics (such as genesis and landfall location, duration, velocity, meridional/zonal movement) and precipitation impacts (magnitude and spatial distribution).